Exchange coupling in (111)-oriented $La_{0.7}Sr_{0.3}MnO_3/La_{0.7}Sr_{0.3}FeO_3$ superlattices

Yue Jia,[1] Rajesh V. Chopdekar,[1] Elke Arenholz,[2] Anthony T. Young,[2] Matthew A. Marcus,[2]
Apurva Mehta,[3] and Yayoi Takamura[1,*]

[1]*Department of Chemical Engineering and Materials Science, University of California, Davis, Davis, California 95616, USA*
[2]*Advanced Light Source, Lawrence Berkeley National Laboratory, Berkeley, California 94720, USA*
[3]*Stanford Synchrotron Radiation Lightsource, SLAC National Accelerator Laboratory, Menlo Park, California 94025, USA*

(Received 15 May 2015; revised manuscript received 17 July 2015; published 3 September 2015)

Epitaxial $La_{0.7}Sr_{0.3}MnO_3$(LSMO)/$La_{0.7}Sr_{0.3}FeO_3$ (LSFO) superlattices serve as model systems to explore the magnetic structure and exchange coupling at (111)-oriented perovskite oxide interfaces. The (111) orientation possesses a buckled honeycomb structure resembling that of graphene with the stacking of highly polar layers. Furthermore, the bulk LSFO magnetic structure suggests that an ideal (111) interface should have fully uncompensated antiferromagnetic (AF) moments leading to exchange bias interactions. Detailed soft x-ray magnetic spectroscopy and microscopy reveal that interfacial effects and ultrathin superlattice sublayers can stabilize orientations of the LSFO AF spin axis, which differ from that of LSFO films and LSMO/LSFO bilayers. A portion of the AF moments can be reoriented to an arbitrary direction by a moderate external magnetic field through spin-flop coupling with the ferromagnetic LSMO sublayers that have low magnetocrystalline anisotropy in the (111) plane.

DOI: 10.1103/PhysRevB.92.094407 PACS number(s): 75.70.Cn, 78.70.Dm, 75.50.Ee

I. INTRODUCTION

Exchange coupling between ferromagnetic (FM) and antiferromagnetic (AF) materials is not only of interest for fundamental research but is also of great significance for industrial applications [1]. Unlike metallic systems that have found wide applications in devices such as hard disk drives, perovskite oxide thin films remain largely in the research arena. The fact that perovskite oxides display a diverse array of functional properties due to the strong correlation between charge, spin, lattice, and orbital degrees of freedom may open new pathways for device applications [2,3]. With advances in deposition techniques, it is possible to fabricate high-quality epitaxial heterostructures with unit cell (u.c.) level control of the layer thickness [4]. However, competing interfacial interactions make it difficult to develop a unified theory to describe the functional properties [5–7]. Until recently, research on perovskite oxide heterostructures has been largely focused on (001)-oriented surfaces, partly due to the difficulty to obtain smooth interfaces on other orientations where different growth mechanisms dominate [8]. Intriguing functional properties possessed by (111)-oriented perovskite thin films that are distinct from (001)-oriented systems have been predicted and discovered by recent theoretical and experimental work [6,9–12]. This new functionality arises due to factors such as the high polarity of the layer stackings and symmetry of the lattice. For example, (001)-oriented $SrTiO_3$ (STO) is composed of neutral layers of SrO and TiO_2 stacked vertically, whereas (111)-oriented STO is composed of highly polar layers of SrO_3^{4-} and Ti^{4+}. The lattice with threefold in-plane rotation symmetry forms a buckled honeycomb structure resembling that of graphene [Fig. 1(b)], which can yield novel electronic and magnetic behaviors.

It has been found that exchange coupling is sensitive to factors such as the surface spins [13], the interfacial roughness [14,15], and the structural and magnetic properties of the constituent layers [16,17]. For idealized planar interfaces with uncompensated AF spins, such as the (111)-plane of a G-type antiferromagnet [Fig. 1(a)], the magnetic moments of the ferromagnet tend to align with the AF spins at the interface to reduce the exchange energy of the system. In this way the FM layer is biased by an exchange bias field, H_E, characterized by a horizontal shift of the magnetic hysteresis loop as well as an enhancement of the coercive field. Interfaces with compensated AF spins, such as the (001)-plane of a G-type antiferromagnet, experience spin frustration where the moments of the FM layer align perpendicularly to the AF spin axis in order to minimize energy. This type of exchange coupling is referred to as spin-flop coupling and is characterized by enhanced coercivity and a lack of horizontal shift of the hysteresis loops [1,18,19]. However, exchange bias is not determined by surface spins alone, and an uncompensated surface is not strictly required [20]. A small fraction of uncompensated pinned spins introduced by atomic-scale interface roughness has been shown to result in exchange bias in some metallic systems [13,15]. For example, J. Nogués *et al.* studied the dependence of the exchange bias field on the interface disorder, crystal orientation, and field cooling direction for the Fe-FeF_2 system [21]. For thin films, they found that exchange bias on the (110) compensated surface decreased as the interface roughness increased (from 0.5–5 nm), while it was absent on the (001) uncompensated surface regardless of interface roughness because the spins of FeF_2 layer lie perpendicular to the interface [21].

Following this notion, we investigated interfacial exchange interactions in (111)-oriented $La_{0.7}Sr_{0.3}MnO_3$ (LSMO)/$La_{0.7}Sr_{0.3}FeO_3$ (LSFO) superlattices. Bulk LSMO is a FM half metal with Curie temperature $T_c \sim 360$ K and saturation magnetization $M_s \sim 3.7\,\mu_B$/Mn [22]. LSMO exhibits colossal magnetoresistance and a high degree of spin polarization. The FM-to-paramagnetic (PM) transition is coincident with the metal-to-insulator transition and meditated by the Mn^{3+}/Mn^{4+} double exchange mechanism [23–25]. Bulk LSFO is a G-type AF insulator with Néel temperature $T_N \sim 360$ K. The electrical

*Corresponding author: ytakamura@ucdavis.edu

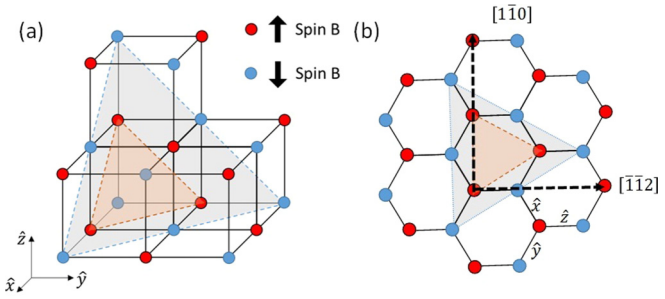

FIG. 1. (Color online) (a) Schematic of a G-type AF perovskite oxide ABO_3 with the A-site cations and oxygen anions omitted. Red and blue spheres represent two sets of B-site cations with antiparallel spins. The red and blue triangles denote (111) planes with all spin up/spin down B-cations. (b) Two-dimensional projection of (111) planes resulting in a honeycomblike structure. $\langle\bar{1}\bar{1}2\rangle$ and $\langle1\bar{1}0\rangle$ are the two low-index families of directions in the (111) plane.

and magnetic properties are meditated by the Fe^{3+}/Fe^{3+} and Fe^{4+}/Fe^{4+} superexchange mechanism [26,27]. Our earlier papers indicated that (001)-oriented LSMO/LSFO superlattices with compensated AF spins at the interface display spin-flop coupling characterized by perpendicular alignment between the AF spin axes and the FM moments at a sublayer thickness of six u.c. [28–30]. In a simple model considering only the expected spin orientation from bulk LSFO with in-plane collinear relation with FM moments and ideally smooth interfaces, the fully uncompensated AF spins in (111)-oriented interfaces should exert an exchange bias on an adjacent FM layer. In this paper, we examine the validity of such a model by using soft x-ray magnetic spectroscopy and microscopy, which can probe FM and AF properties separately using the element specificity of the technique. We have found that the spin axis of LSFO in the superlattice cants out-of-plane of the surface in contrast to LSFO films and LSMO/LSFO bilayers, indicating that the spin coupling in a multilayer is more complex.

II. EXPERIMENTAL PROCEDURE

LSMO/LSFO superlattices consisting of alternating layers of 9 u.c. of LSMO and 9 u.c. of LSFO repeated 10 times (referred to as $[9 \times 9]10$) were grown on (111)-oriented STO substrates by pulsed laser deposition. The LSMO layer was grown first so that the LSFO layer lies at the film surface. For comparison, single-layer films of LSMO (27 nm) and LSFO (34 nm), as well as a LSMO/LSFO bilayer (60 u.c. for each layer, and referred to as $[60 \times 60]1$), were also grown. The substrates were treated with only a solvent clean to remove organic residue from the surface. A KrF laser (248 nm) was used with a frequency of 5 Hz (1 Hz) and fluence of $\sim 0.5\,J\,cm^{-2}$ ($\sim 0.9\,J\,cm^{-2}$) for the growth of the LSMO (LSFO) layers. The substrate was held at 700 °C, and the oxygen pressure was 300 mTorr. The samples were cooled slowly to room temperature after the deposition with an oxygen pressure of 300 Torr to ensure the proper oxygen stoichiometry.

The layer and sublayer properties were characterized by high resolution x-ray diffraction (HRXRD) and resonant x-ray reflectivity (XRR) measurements using a Bruker D8 Discover four-circle diffraction system and Beamline 2-1 at the Stanford Synchrotron Radiation Lightsource (SSRL). Due to the small density contrast between the sublayers in the superlattice when using a conventional Cu lab x-ray source, resonant XRR was performed at energies near the Mn and Fe K edges, 6556 eV and 7127 eV, respectively, and 8000 eV as a reference away from the Mn and Fe absorption edges. This technique provides a nondestructive means of determining chemical profiles of multilayer structures (i.e., chemical intermixing or diffusion between individual sublayers) [31].

The sublayer thickness, roughness, and density were obtained by simulating the resonant XRR spectra using Leptos software from Bruker AXS [32]. Leptos accounts for the real and imaginary parts of the dispersion correction factor, f' and f'', when calculating XRR. f' and the Thomson scattering amplitude, f_0, display a strong energy dependence and decrease sharply at absorption edges [31]. The bulk magnetization was measured using a Quantum Design superconducting quantum interface device (SQUID) magnetometer with the magnetic field applied along the in-plane $[1\bar{1}0]$ direction. Soft x-ray magnetic spectroscopy measurements were performed at Beamlines 4.0.2 and 6.3.1 of the Advanced Light Source (ALS) using total electron yield mode. The x-ray magnetic circular dichroism (XMCD) measurements were performed at 80 K with the x rays at 30° grazing incidence, with the in-plane projection along either the $[\bar{1}10]$ or $[11\bar{2}]$ directions, and a magnetic field of ± 0.5 T applied along the x-ray beam direction in order to probe the magnetic behaviors of the FM LSMO layers in the superlattice and the single layer LSMO film. Magnetic characterization of the AF LSFO layers was carried out using x-ray magnetic linear dichroism (XMLD), which is sensitive to anisotropy arising from crystallographic, electronic, and magnetic effects. A detailed angular-dependent study of Fe $L_{2,3}$ XMLD was carried out at 80 K with two variants of measurements, whose detailed geometries will be described below. Soft x-ray photoemission electron microscopy (X-PEEM) images were obtained at 100 K after zero-field cooling using the PEEM3 microscope on Beamline 11.0.1 at the ALS. The x rays impinged upon the sample at 30° grazing incidence with the in-plane projection along the $[\bar{1}10]$ direction.

III. RESULTS AND DISCUSSION

A. Structural characterization

The experimental resonant XRR spectra (colored) as a function of scattering vector for the (111)-oriented $[9 \times 9]10$ superlattice are shown in Fig. 2 along with the simulated curves (black). Pronounced thickness fringes are observed for all three x-ray energies and persist to large scattering vector values (up to $0.9\,Å^{-1}$). Distinct superlattice peaks with a periodicity of 4.4 nm were observed using x-ray energies near the Mn and Fe K edges and indicated by arrows in Fig. 2 but are subtle at 8000 eV where the $f' + f_0$ values for LSMO and LSFO are nearly identical. All of the LSMO (LSFO) layers are simulated with the same parameters listed in Table I obtained with Leptos software [32] with the density of the STO substrate fixed at the theoretical value. Most of the resonant spectral features indicated by the arrows can be reproduced. The cost function is a measure of the overall goodness of the fit of the simulation to the experimental data. A thin carbon top layer that might form due to exposure to x rays in air was also included to improve the fitting. Slightly different fitting parameters for the

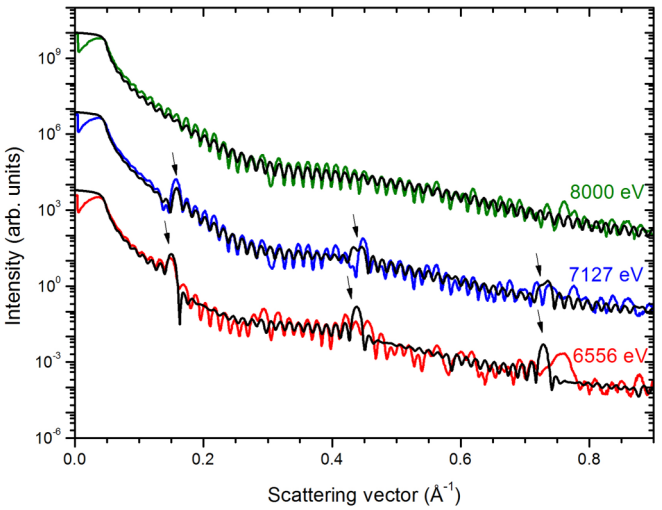

FIG. 2. (Color online) Experimental (colored) and simulated (black) XRR spectra acquired with x-ray energies of 8000 eV, 7127 eV (near Fe K edge), and 6556 eV (near Mn K edge). Optimized parameters used to simulate XRR spectra are listed in Table I. Features in resonant XRR spectra corresponding to a periodicity of 4.4 nm are indicated by arrows.

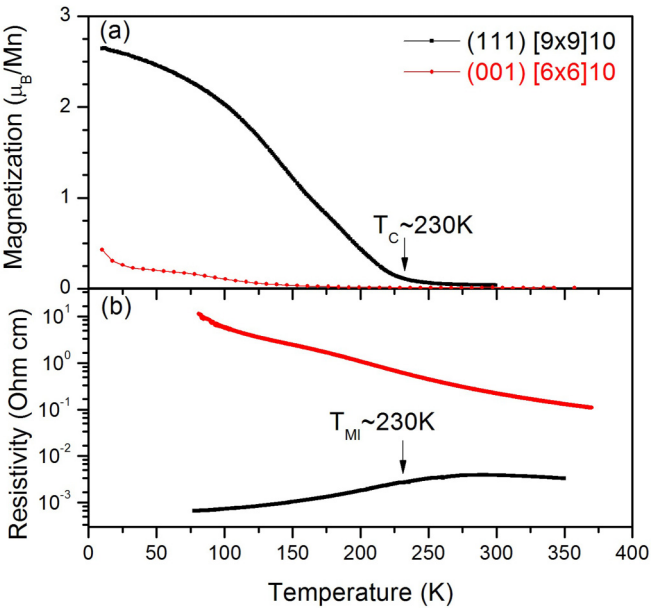

FIG. 3. (Color online) Temperature dependence of (a) magnetization and (b) resistivity for a (111)-oriented [9 × 9]10 superlattice and (001)-oriented [6 × 6]10 superlattice.

carbon layer were used at each x-ray energy. The fitting results reveal that the superlattice has the desired sublayer thickness and smooth interfaces with limited chemical intermixing or diffusion between sublayers.

Clear thickness fringes due to finite thickness effects were also present in ω-2θ scans of the (111)-oriented [9 × 9]10 superlattice, the LSMO and LSFO single layer films, and the LSMO/LSFO bilayer as measured near the (111) and (222) peaks (not shown), which confirms their high degree of crystallinity with smooth interfaces. Reciprocal space maps around the 042 and 330 reflections (not shown) show that all the films are crystalline, fully strained, and coherent to the underlying STO substrate. Assuming pseudocubic lattice parameters of $a_{pc} = 3.87$ Å for LSMO [33] and $a_{pc} = 3.91$ Å for LSFO [34], LSMO and LSFO are under 0.9% in-plane tensile strain and 0.15% in-plane compressive strain, respectively. These results confirm the high structural quality of all the (111)-oriented samples.

B. Bulk magnetic and electrical properties

Figure 3 plots the temperature dependence of the magnetization [Fig. 3(a)] and resistivity [Fig. 3(b)] of the (111)-oriented [9 × 9]10 superlattice compared with (001)-oriented [6 × 6]10 superlattices with equivalent sublayer thickness (2.3 nm) [29]. The magnetization curves were measured with an applied field of 0.01 T along the in-plane [1$\bar{1}$0] direction after zero-field cooling from room temperature and were normalized to the thickness of the LSMO layer only. The resistivity was measured using the van der Pauw geometry, and it was calculated using the thickness of the entire superlattice rather than the conductive LSMO layers only.

Both the magnetization and resistivity curves for the (111)-oriented [9 × 9]10 superlattice show the expected behavior consisting of coincident FM-to-PM and metal-to-insulator transitions at a reduced $T_c \sim 230$ K $\sim T_{MI}$ compared to bulk. T_{MI} is defined at the maximum $\frac{d\rho}{dT}$. In comparison, the (001)-oriented [6 × 6]10 superlattice displayed purely insulating behavior over the entire temperature range studied and a significantly suppressed saturation magnetization value [0.57 μ_B/Mn for the (001)-oriented [6 × 6]10 superlattice and 2.8 μ_B/Mn for the (111)-oriented [9 × 9]10 superlattice].

In ultrathin films, the suppression of M_s and T_c has been attributed to factors such as epitaxial strain [35,36], orbital ordering [37], and surface and interfacial effects [38]. MnO_6 octahedra distortions and rotations caused by epitaxial

TABLE I. Optimized fit parameters for resonant XRR spectra

	Thickness (nm)	Roughness (nm)	Density (g cm^{-3})	Theoretical density (g cm^{-3})
Carbon layer[a]	1.1 ∼ 1.3	0.3 ∼ 0.4	1.7 ∼ 2.1	N/A
LSFO	2.13	0.21	6.24	6.31
LSMO	2.18	0.19	6.34	6.46
STO (sub)		0.17	5.12	5.12
Energy (eV)	6556	7127	8000	
Cost function	1.0×10^{-1}	7.1×10^{-2}	4.7×10^{-2}	

[a]Slightly different fitting parameters of the carbon capping layer were used for each x-ray energy.

strain change the $Mn^{3+} - O - Mn^{4+}$ bond length and bond angle, which can significantly affect the e_g electron hopping integral. One possible reason for the differences in the M_s, T_c, and resistivity values for the (001)-oriented [6 × 6]10 superlattice and the (111)-oriented [9 × 9]10 superlattice can be attributed to the different ways the BO_6 octahedra distort and rotate due to epitaxial strain, as well as the difference in octahedral truncation across the (001)- and (111)-interfaces. The (001)-interface truncates the octahedra at the vertices, while the (111)-interface truncates the octahedra on the faces. This may result in different influences on the double exchange mechanism, leading to drastically different magnetic and electrical properties [39].

C. XMCD spectroscopy

To study interfacial effects on the magnetic properties of the LSMO and LSFO layers in the (111)-oriented [9 × 9]10 superlattice, Mn and Fe $L_{2,3}$ x-ray absorption (XA) and XMCD spectra were acquired. XMCD is defined as the difference between two XA spectra with antiparallel and parallel orientations of the sample magnetization and incident photon spin and is a measure of the atomic spin and orbital magnetic moment. No Fe XMCD signal was observed, indicating that no or few uncompensated Fe spins exist in the LSFO layers. Figure 4 shows that the Mn $L_{2,3}$ XA and XMCD spectra of the [9 × 9]10 superlattice and LSMO film are similar except for a more pronounced shoulder in the XA spectra on the low energy side of the L_3 peak and a slight shift of the main L_3 peak to higher energy for the superlattice. These features have been attributed to a higher Mn^{4+}/Mn^{3+} ratio than expected for the Sr doping level [40,41]. Due to the uniform Sr^{2+} doping through the entire superlattice, this change in the Mn valence state is believed to result from the transfer of an electron from Mn^{3+} to Fe^{4+} across the interfaces [42]. This charge transfer was also observed in (001)-oriented LSMO/LSFO superlattices [29] and can explain the suppression of M_s and T_c from bulk LSMO values. The valence change due to this interfacial effect is equivalent to the higher Sr^{2+} doping level for LSMO, which results in a FM with reduced M_s and T_c [43].

The Mn XMCD hysteresis loops of the [9 × 9]10 superlattice and the LSMO film are shown in Fig. 4(b). The asymmetry values were determined as the difference between the absorption values of right and left circularly polarized x rays at the photon energy corresponding to the maximum in XMCD, normalized to their sum. The hysteresis loops of the superlattice with the magnetic field applied along the in-plane [11$\bar{2}$] and [1$\bar{1}$0] directions [i.e., two low-index families of directions lying in the (111)-plane] display little difference, suggesting that the magnetocrystalline anisotropy within the (111)-plane is small. The Mn XMCD hysteresis loops show differences in the shape as well as the coercive field (1 mT for the LSMO film and 4 mT for the [9 × 9]10 superlattice), and this coercivity enhancement is a signature of exchange coupling. These coercivity values obtained from Mn XMCD measurements are reproduced in hysteresis loops taken with SQUID magnetometry. Comparison of the SQUID hysteresis loops of the superlattice measured at 10 K after zero-field cooling and 2 T field cooling from 300 K along the [1$\bar{1}$0] and [11$\bar{2}$] directions do not show any horizontal shifts of the field-cooled loops, which suggests the absence of exchange bias in the superlattice.

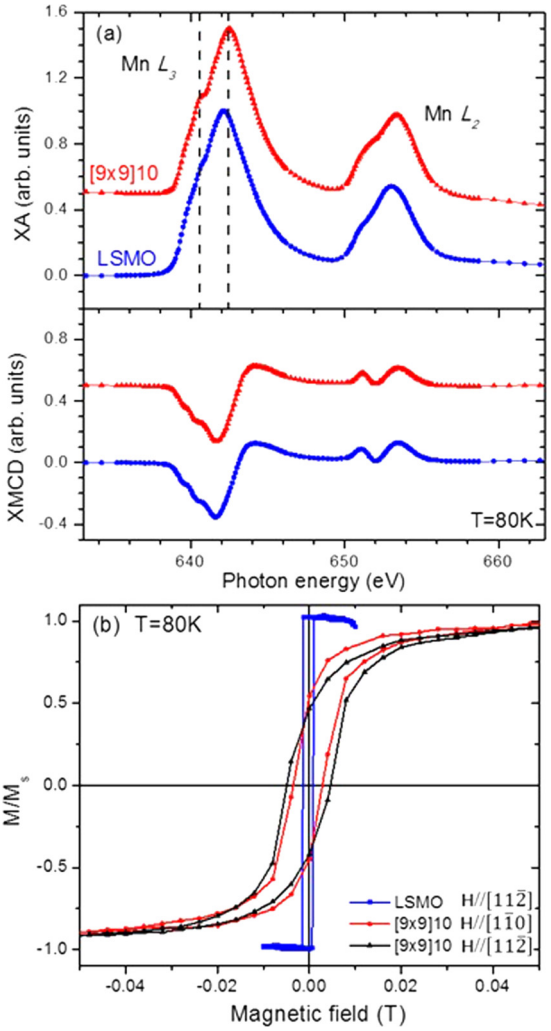

FIG. 4. (Color online) (a) Mn XA and XMCD spectra and (b) Mn XMCD hysteresis loops for the (111)-oriented [9 × 9]10 superlattice and LSMO thin film.

D. XMLD spectroscopy and microscopy

The lack of exchange bias may result from deviations of the magnetic structure of the ultrathin LSFO layers in the superlattice compared to bulk samples. Hence, the magnetic structure was investigated systematically using XMLD spectroscopy and microscopy. The AF spin axis of bulk LSFO lies along the crystallographic ***a*** axis [26], while reports on the AF spin axis of (001)-oriented LSFO thin films vary with growth conditions and strain state. The previous study on (001)-oriented [6 × 6]10 LSMO/LSFO superlattices suggested that the AF spin axis lies in the plane of the film along ⟨100⟩ directions and perpendicular to the LSMO moment. In contrast, (001)-oriented LSFO thin films grown with the same deposition conditions and strain state have an AF spin axis that cants out-of-plane by ∼30° [29,30,44]. Interfacial effects are believed to play a significant role on determining the spin axis orientation of the AF layers. In order

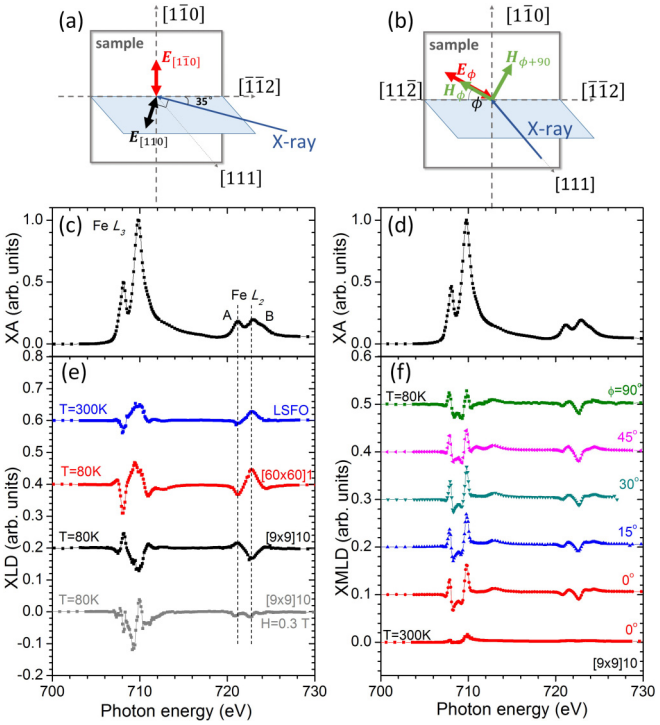

FIG. 5. (Color online) (a), (b) Schematics of the two XMLD measurement geometries; (c), (d) XA spectra of the (111)-oriented [9 × 9]10 superlattice measured in (c) geometry 1 and (d) geometry 2 with $\phi = 0°$. (e) Comparison of XMLD(1) spectra for three (111)-oriented samples; the (111)-oriented [9 × 9]10 superlattice was measured without (black) and with (gray) a magnetic field of 0.3 T applied along the x-ray beam direction. (f) ϕ angular dependence of XMLD(2) spectra of the (111)-oriented [9 × 9]10 superlattice.

to determine the AF spin axis of LSFO in the (111)-oriented [9 × 9]10 superlattice as well as the nature of the coupling between the LSFO and LSMO layers, Fe XMLD spectra were measured in two different geometries.

In geometry 1 [Fig. 5(a)], Fe XMLD spectra were acquired at 35° grazing incidence with $\boldsymbol{H} = 0$ after zero-field cooling the sample from room temperature. The x-ray polarization, $\boldsymbol{E}$, either lies in the plane of sample surface along the [110] direction or cants out-of-plane along the [1$\bar{1}$0] direction. These two directions belong to the same family of crystallographic directions, thereby minimizing crystal field effects on the linear dichroism spectra. The XMLD spectrum is defined as

$$I_{\mathrm{XMLD(1)}} = I_{\mathrm{XA}}(\boldsymbol{E}_{[110]}) - I_{\mathrm{XA}}(\boldsymbol{E}_{[1\bar{1}0]}), \qquad (1)$$

and is indicative of the orientation of the LSFO spin axis relative to the sample surface.

In geometry 2 [Fig. 5(b)], the x rays are incident upon the sample at normal incidence, and the x-ray polarization $\boldsymbol{E}$ rotates from the [11$\bar{2}$] to [1$\bar{1}$0] directions. A magnetic field of $\boldsymbol{H} = 0.3$ T is applied parallel or perpendicular to $\boldsymbol{E}$. The XMLD spectrum at normal incidence is defined as

$$I^{\mathrm{normal}}_{\mathrm{XMLD(2)}}(\phi) = I_{\mathrm{XA}}(\boldsymbol{H}_\phi, \boldsymbol{E}_\phi) - I_{\mathrm{XA}}(\boldsymbol{H}_{\phi+90}, \boldsymbol{E}_\phi), \qquad (2)$$

where the subscripts of $\boldsymbol{H}$ and $\boldsymbol{E}$ indicate the angle of these vectors with respect to the in-plane [11$\bar{2}$] direction. The magnetic field orients the Mn moments parallel or perpendicular to $\boldsymbol{E}$, thus the Fe XMLD spectrum indicates the response of the Fe moments to the change of Mn moment orientation through exchange coupling. The presence or lack of angular dependence of this XMLD spectrum sheds light on the role of crystal anisotropy on the exchange coupling interaction. A full understanding of the crystal anisotropy requires additional modeling, which is beyond the scope of this paper.

Figures 5(c) and 5(e) plot the Fe $L_{2,3}$ XA and XMLD(1) spectra for the (111)-oriented [9 × 9]10 superlattice, the [60 × 60]1 bilayer, and the single layer LSFO film. The XA spectra for the three samples are nearly identical in spite of the charge transfer from Mn, since for low Sr doping it has been shown that the O 2p states are modified rather than the Fe 3d states [40]. However, the XMLD(1) spectra display distinct differences in magnitude and sign. The XMLD(1) spectra of the bilayer and single layer LSFO have similar shape with negative/positive peaks at the L_{2A}/L_{2B} energies, respectively. In contrast, the sign is reversed for the superlattice, which suggests that the orientation of the AF spin axes of the superlattice differs from that of the thicker LSFO layers. A similar result was found for the (001)-oriented [6 × 6]10 LSMO/LSFO superlattices, where a sign reversal of the Fe XMLD spectra was indication of an in-plane alignment of the LSFO spin axis in the superlattice and the out-of-plane canting in the LSFO single layer film [29]. The Fe $L_{2,3}$ XMLD(1) spectrum for the (111)-oriented [9 × 9]10 superlattice was also obtained with a magnetic field $\boldsymbol{H} = 0.3$ T applied along the x-ray beam direction shown in Fig. 5(e). In the absence of spin-flop coupling, this value of magnetic field is too small to rotate the AF spin axis directly but sufficient to orient all of the Mn moments, as seen from the hysteresis loops in Fig. 4. In the presence of spin-flop coupling, the Fe AF spins are forced to rotate to maintain a perpendicular orientation to the Mn moments. The observed significant change of the spectra with applied magnetic field suggests a reorientation of the AF spins compared to the demagnetized state.

X-PEEM images allow us to confirm the orientation of the LSFO spin axis in the superlattices and the bilayer in a spatially resolved manner. The images shown in Fig. 6 were obtained by taking the ratio between images taken at the Fe L_{2A} and L_{2B} peaks for a given x-ray polarization as it rotates from parallel to or perpendicular to the plane of incidence. This procedure removes contributions from the surface topography and enhances the AF contrast. The AF domain contrast arises from the Fe XMLD effect, and the intensity has a $\cos^2\theta$ dependence, where θ is the angle between $\boldsymbol{E}$ and the AF spin axis. Therefore, the image contrast is strongest between AF domains with the spin axis parallel with and perpendicular to $\boldsymbol{E}$. The X-PEEM measurement geometry is shown in Fig. 6(a), with φ defined as the angle between $\boldsymbol{E}$ and the plane of incidence. Figures 6(b)–6(e) show the X-PEEM images acquired for the [9 × 9]10 superlattice with $\varphi = 0$, i.e., p polarization ($\boldsymbol{E}$ parallel with the plane of incidence and canting out-of-the sample plane by 60°), $\varphi = 30°$, $\varphi = 60°$, and $\varphi = 90°$, i.e., s polarization ($\boldsymbol{E}$ perpendicular to the plane of incidence and lying in the sample plane along the [$\bar{1}\bar{1}$2] direction). For the case that the AF spin axis cants out-of-plane, the $\varphi = 90°$ domain image will have weak contrast since the AF spin axis in all domains are nearly

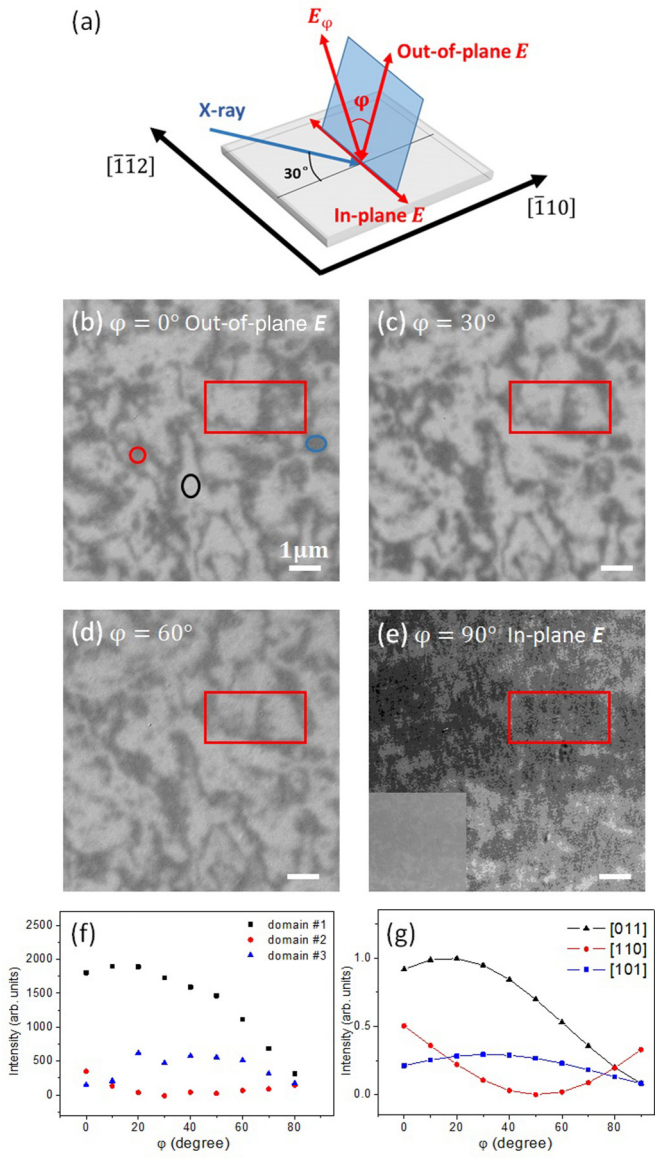

FIG. 6. (Color online) (a) Measurement geometry of X-PEEM. φ is defined as the angle between the x-ray polarization and the plane of incidence. (b)–(e) AF domain image of the (111)-oriented [9 × 9]10 superlattice taken at 100 K with (b) $\varphi = 0^\circ$ (out-of-plane $\boldsymbol{E}$), (c) $\varphi = 30^\circ$, (d) $\varphi = 60^\circ$, and (e) $\varphi = 90^\circ$ (in-plane $\boldsymbol{E}$). The contrast in (e) has been enhanced in order to more clearly see the features, while the inset shows the image at the same contrast level as in (b)–(d). (f) The variation of the intensity with φ for three domains circled in Fig. 6(b) (black: domain #1; red: domain #2; and blue: domain #3). (g) The calculated intensity for domains with the AF spin axis along the [011], [110], and [101] directions.

perpendicular to the in-plane $\boldsymbol{E}$ vector, while strong contrast will be observed for $\varphi < 90^\circ$ when the $\boldsymbol{E}$ vector lies close to parallel (perpendicular) to the AF spin axes in neighboring domains. The value of φ where the maximum contrast occurs is indicative of the canting angle of the AF spin axes.

For the [9 × 9]10 superlattice, the domain contrast is strong for $\varphi = 0$ and gradually decreases as $\boldsymbol{E}$ rotates in-plane {i.e., φ increases [Figs. 6(b)–6(e)]}. For the bilayer (not shown), the φ dependence is reversed, with strong contrast for $\varphi = 90^\circ$ and weak for $\varphi = 0^\circ$. This behavior is consistent with the sign reversal of the Fe XMLD(1) spectra shown in Fig. 5. The area indicated by the red boxes in Figs. 6(b)–6(e) highlights the complex domain behavior in the (111)-oriented samples. The large white domain on the left-hand side of the image for $\varphi = 0^\circ$ is seen to actually be composed of multiple small domains as φ increases. Figure 6(f) plots the intensity of three domains circled in Fig. 6(b) (black: domain #1; red: domain #2; and blue: domain #3) as a function of x-ray polarization angle, while Fig. 6(g) shows the predictions based on a $\cos^2\theta$ dependence for domains with the AF spin axis oriented along the [011], [110], and [101] directions, which cant out-of-plane by 55°. A good agreement between the experimental and model curves can be observed in terms of the shape of the curves and the approximate φ angle where the curves intersect. Unlike the (001)-oriented [6 × 6]10 superlattice [30], a direct one-to-one correspondence between AF and FM domain patterns was not observed, but rather only a local correspondence exists between the location of AF and FM domain walls.

The Fe $L_{2,3}$ XA spectrum with $\phi = 0^\circ$ and XMLD(2) spectra with $\phi = 0^\circ$, 15°, 30°, 45°, and 90° of the (111)-oriented [9 × 9]10 superlattice are shown in Figs. 5(d) and 5(f). In this case, the x rays impinge onto the sample at normal incidence, and the XMLD spectra probe the response of the in-plane component of the LSFO spin axis to the external field through exchange coupling. The applied magnetic field aligns the Mn moments either parallel with or perpendicular to the x-ray $\boldsymbol{E}$ vector. To confirm that the reorientation of the Fe moments indicated by the observed Fe XMLD(2) signal is due to spin-flop coupling with the Mn moments, Fe XMLD(2) spectra with $\phi = 0^\circ$ were acquired both at room temperature above T_c of the superlattice and at 80 K. The Fe XMLD signal vanishes at room temperature as expected. By varying ϕ, the effect of crystal symmetry can be studied. In the (001)-oriented superlattice, clear spectral differences were observed for spectra along the two low index directions lying in-plane (i.e., ⟨100⟩ and ⟨110⟩ directions); however, in the present case, no significant difference between the Fe XMLD spectra varying ϕ was observed. This result suggests that the crystalline anisotropy is low along the ⟨1̄1̄2⟩ and ⟨1̄10⟩ directions lying within the (111) plane. This behavior is consistent with the low magnetocrystalline anisotropy of the LSMO layers measured by Mn XMCD, which has been observed in (111)-oriented single layer LSMO film [45].

Therefore, the XMLD measurements demonstrate that the AF spin axis in the (111)-oriented superlattice deviates from the expected bulk structure by canting out-of-plane with a canting angle consistent with the low-index ⟨110⟩ directions. This interfacial spin configuration results from the competition of factors such as the anisotropy of the FM and AF layers, the strength of exchange coupling at the top and bottom of the AF layers, and the presence of defects at the interfaces. Previous experimental [21] and theoretical work [20,46] has shown that an out-of-plane canting of the AF spin axis results in an absence of exchange bias in order to minimize the energy difference between parallel and antiparallel configurations between the FM moments and the in-plane component of the AF spins. Furthermore, the observed perpendicular coupling was found to become more energetically favorable in the presence of interface roughness or domain formation in the

Fe-FeF_2 system. In comparison to the (001)-oriented $[6 \times 6]10$ superlattice, the XMLD(2) signal is reduced by a factor of four at the L_{2B} peak. A part of the signal reduction comes from the out-of-plane canting of the AF spin axis while the XMLD(2) geometry only probes the in-plane projection. It is also possible that only part of the AF spins are spin-flop coupled with the LSMO layers [29]. The remaining decoupled spins are likely to be in domain walls and pinned by crystalline defects (i.e., twin boundaries [47]) and cannot be rotated.

IV. CONCLUSIONS

In summary, the magnetic interactions in (111)-oriented LSMO/LSFO superlattices have been systematically studied. Comparison to their (001)-oriented counterparts indicates that the magnetic structure in these multilayers is significantly different. Robust ferromagnetism and transport behavior were maintained in the (111)-orientation at an ultrathin sublayer thickness of 2.2 nm. The absence of exchange bias in these samples implies that a simple spin structure diagram derived from the bulk magnetic structure cannot be assumed to hold at these small thicknesses and in the presence of a high density of interfaces. Rather, soft x-ray magnetic spectroscopy and microscopy show that the spin axis of LSFO cants out-of-the plane in the LSMO/LSFO superlattice, likely along the ⟨110⟩ directions, while it lies in-plane for a bilayer with a thick LSFO layer without a high density of interfaces. In this case, a portion of AF spins can be reoriented by a moderate external magnetic field through spin-flop coupling with LSMO, and the coupling is isotropic and independent of the in-plane crystalline direction.

ACKNOWLEDGMENTS

This paper was supported by the Semiconductor Research Corporation under Task No. 2309.001. The Advanced Light Source is supported by the Director, Office of Science, Office of Basic Energy Sciences, of the U.S. Department of Energy under Contract No. DE-AC02-05CH11231. Use of the Stanford Synchrotron Radiation Lightsource, SLAC National Accelerator Laboratory, is supported by the U.S. Department of Energy, Office of Science, Office of Basic Energy Sciences under Contract No. DE-AC02-76SF00515.

[1] J. Nogués, J. Sort, V. Langlais, V. Skumryev, S. Suriñach, J. S. Muñoz, and M. D. Baró, Phys. Rep. **422**, 65 (2005).
[2] P. Zubko, S. Gariglio, M. Gabay, P. Ghosez, and J.-M. Triscone, Annual Review of Condensed Matter Physics **2**, 141 (2011).
[3] R. Ramesh and N. A. Spaldin, Nat. Mater. **6**, 21 (2007).
[4] H. M. Christen and G. Eres, J. Phys.: Condens. Matter **20**, 264005 (2008).
[5] M. Blamire and B. Hickey, Nat. Mater. **5**, 87 (2006).
[6] M. Gibert, P. Zubko, R. Scherwitzl, J. Íñiguez, and J.-M. Triscone, Nat. Mater. **11**, 195 (2012).
[7] S. Dong, K. Yamauchi, S. Yunoki, R. Yu, S. Liang, A. Moreo, J.-M. Liu, S. Picozzi, and E. Dagotto, Phys. Rev. Lett. **103**, 127201 (2009).
[8] I. Hallsteinsen, J. E. Boschker, M. Nord, S. Lee, M. Rzchowski, P. E. Vullum, J. K. Grepstad, R. Holmestad, C. B. Eom, and T. Tybell, J. Appl. Phys. **113**, 183512 (2013).
[9] D. Doennig, W. E. Pickett, and R. Pentcheva, Phys. Rev. Lett. **111**, 126804 (2013).
[10] K. Ueda, Science **280**, 1064 (1998).
[11] K. Ueda, H. Tabata, and T. Kawai, Phys. Rev. B **60**, R12561 (1999).
[12] A. Grutter, F. Wong, E. Arenholz, M. Liberati, A. Vailionis, and Y. Suzuki, Appl. Phys. Lett. **96**, 082509 (2010).
[13] H. Ohldag, A. Scholl, F. Nolting, E. Arenholz, S. Maat, A. T. Young, M. Carey, and J. Stöhr, Phys. Rev. Lett. **91**, 017203 (2003).
[14] M. D. Stiles and R. D. McMichael, Phys. Rev. B **59**, 3722 (1999).
[15] W. Kuch, L. I. Chelaru, F. Offi, J. Wang, M. Kotsugi, and J. Kirschner, Nat. Mater. **5**, 128 (2006).
[16] M. S. Lund, W. A. A. Macedo, K. Liu, J. Nogués, I. K. Schuller, and C. Leighton, Phys. Rev. B **66**, 054422 (2002).
[17] S. Maat, K. Takano, S. S. P. Parkin, and E. E. Fullerton, Phys. Rev. Lett. **87**, 087202 (2001).
[18] M. Finazzi, Phys. Rev. B **69**, 064405 (2004).
[19] N. C. Koon, Phys. Rev. Lett. **78**, 4865 (1997).
[20] A. P. Malozemoff, Phys. Rev. B **35**, 3679 (1987).
[21] J. Nogués, T. J. Moran, D. Lederman, I. K. Schuller, and K. V. Rao, Phys. Rev. B **59**, 6984 (1999).
[22] A. Urushibara, Y. Moritomo, T. Arima, A. Asamitsu, G. Kido, and Y. Tokura, Phys. Rev. B **51**, 14103 (1995).
[23] P. de Gennes, Phys. Rev. **118**, 141 (1960).
[24] P. Anderson and H. Hasegawa, Phys. Rev. **100**, 675 (1955).
[25] A. J. Millis, P. B. Littlewood, and B. I. Shraiman, Phys. Rev. Lett. **74**, 5144 (1995).
[26] R. L. White, J. Appl. Phys. **40**, 1061 (1969).
[27] U. Shimony and J. M. Knudsen, Phys. Rev. **144**, 361 (1966).
[28] E. Arenholz, G. van der Laan, F. Yang, N. Kemik, M. D. Biegalski, H. M. Christen, and Y. Takamura, Appl. Phys. Lett. **94**, 072503 (2009).
[29] Y. Takamura, F. Yang, N. Kemik, E. Arenholz, M. D. Biegalski, and H. M. Christen, Phys. Rev. B **80**, 180417 (2009).
[30] F. Yang, N. Kemik, A. Scholl, A. Doran, A. T. Young, M. D. Biegalski, H. M. Christen, and Y. Takamura, Phys. Rev. B **83**, 014417 (2011).
[31] N. Kemik, M. Gu, F. Yang, C. Y. Chang, Y. Song, M. Bibee, A. Mehta, M. D. Biegalski, H. M. Christen, N. D. Browning, and Y. Takamura, Appl. Phys. Lett. **99**, 201908 (2011).
[32] *Leptos Manual* (Bruker AXS, Wisconson, 2005).
[33] P. G. Radaelli, G. Iannone, M. Marezio, H. Y. Hwang, S.-W. Cheong, J. D. Jorgensen, and D. N. Argyriou, Phys. Rev. B **56**, 8265 (1997).
[34] A. Fossdal, M. Menon, I. Waernhus, K. Wiik, M. A. Einarsrud, and T. Grande, J. Am. Ceram. Soc. **87**, 1952 (2004).
[35] C. Adamo, X. Ke, H. Q. Wang, H. L. Xin, T. Heeg, M. E. Hawley, W. Zander, J. Schubert, P. Schiffer, D. A. Muller, L. Maritato, and D. G. Schlom, Appl. Phys. Lett. **95**, 112504 (2009).

[36] F. Yang, N. Kemik, M. D. Biegalski, H. M. Christen, E. Arenholz, and Y. Takamura, Appl. Phys. Lett. **97**, 092503 (2010).
[37] M. Huijben, L. W. Martin, Y. H. Chu, M. B. Holcomb, P. Yu, G. Rijnders, D. H. A. Blank, and R. Ramesh, Phys. Rev. B **78**, 094413 (2008).
[38] J. Z. Sun, D. W. Abraham, R. A. Rao, and C. B. Eom, Appl. Phys. Lett. **74**, 3017 (1999).
[39] H. Boschker, J. Kautz, E. P. Houwman, W. Siemons, D. H. A. Blank, M. Huijben, G. Koster, A. Vailionis, and G. Rijnders, Phys. Rev. Lett. **109**, 157207 (2012).
[40] M. Abbate, F. M. F. de Groot, J. C. Fuggle, A. Fujimori, O. Strebel, F. Lopez, M. Domke, G. Kaindl, G. A. Sawatzky, M. Takano, Y. Takeda, H. Eisaki, and S. Uchida, Phys. Rev. B **46**, 4511 (1992).
[41] F. De Groot, J. Electron Spectrosc. Relat. Phenom. **67**, 529 (1994).
[42] H. Kumigashira, D. Kobayashi, R. Hashimoto, A. Chikamatsu, M. Oshima, N. Nakagawa, T. Ohnishi, M. Lippmaa, H. Wadati, and A. Fujimori, Appl. Phys. Lett. **84**, 5353 (2004).
[43] Y. Tokura and Y. Tomioka, J. Magn. Magn. Mater. **200**, 1 (1999).
[44] Y. Takamura, in *Nanostructured Materials for Magnetoelectronics*, edited by B. Aktaş and F. Mikailzade (Springer, Berlin Heidelberg, 2013).
[45] I. Hallsteinsen, E. Folven, F. Olsen, R. Chopdekar, M. Rzchowski, C. Eom, J. Grepstad, and T. Tybell, APL Materials **3**, 062501 (2015).
[46] A. P. Malozemoff, J. Appl. Phys. **63**, 3874 (1988).
[47] J. W. Seo, C. Dieker, J. Fompeyrine, H. Siegwart, and J.-P. Locquet, International Journal of Materials Research **97**, 943 (2006).